Controlling interactions between high-frequency phonons and single quantum systems using phononic crystals

Kuruma, Kazuhiro; Pingault, Benjamin; Chia, Cleaven; Haas, Michael; Joe, Graham D.; Assumpcao, Daniel Rimoli; Ding, Sophie Weiyi; Jin, Chang; Xin, C. J.; Yeh, Matthew

DOI
10.1038/s41567-024-02697-5

Publication date
2024

Document Version
Final published version

Published in
Nature Physics

nature physics

Article

https://doi.org/10.1038/s41567-024-02697-5

Controlling interactions between high-frequency phonons and single quantum systems using phononic crystals

Received: 9 October 2023

Accepted: 7 October 2024

Published online: 18 December 2024

Check for updates

Kazuhiro Kuruma[1,2] ✉, Benjamin Pingault[1,3,4,5], Cleaven Chia[1], Michael Haas[1], Graham D. Joe[1], Daniel Rimoli Assumpcao[1], Sophie Weiyi Ding[1], Chang Jin[1], C. J. Xin[1], Matthew Yeh[1], Neil Sinclair[1] & Marko Lončar[1] ✉

The ability to control phonons in solids is key in many fields of quantum science, ranging from quantum information processing to sensing. Phonons often act as a source of noise and decoherence when solid-state quantum systems interact with the phonon bath of their host matrix. In this study, we demonstrate the ability to control the phononic local density of states of the host matrix using phononic crystals and measure its positive impact on single quantum systems. We design and fabricate diamond phononic crystals with features down to around 20 nm, resulting in a high-frequency complete phononic bandgap from 50 to 70 GHz. The engineered local density of states is probed using single silicon-vacancy colour centres embedded in the phononic crystals. We observe an 18-fold reduction in the phonon-induced orbital relaxation rate of the emitters compared to bulk, thereby demonstrating that the phononic crystal suppresses spontaneous single-phonon processes. Furthermore, we show that our approach can efficiently suppress single-phonon–emitter interactions up to 20 K, allowing the investigation of multi-phonon processes in the emitters. Our results represent an important step towards the realization of efficient phonon–emitter interfaces that can be used for quantum acoustodynamics and quantum phononic networks.

Engineering the interactions of quantum systems with phonons/vibrations is an important task for a wide range of disciplines, including quantum information[1–3], optoelectronics[4], metrology[5], energy harvesting[6] and sensing[7,8]. Although coherent phonons can play an important role as carriers of quantum information[9,10], thermal phonons can negatively impact the properties of quantum systems, even at single-phonon levels, and eventually limit the performance of quantum devices[11–13]. The most common approach to address this issue is to decrease the thermal phonon population by operating at cryogenic temperatures, down to the millikelvin range[9,14,15]. However, this approach requires complex and expensive cryogenic systems and does not prevent phonon modes from being repopulated through local heating from driving fields used to interact with the quantum system[16,17]. Furthermore, this approach, solely based on Boltzmann statistics, does not allow precise control of the phononic local density of states (LDOS) to target specific frequency ranges. The latter may be important for locally suppressing or enhancing interactions between targeted phonons and quantum systems. Therefore, it is important

[1]John A. Paulson School of Engineering and Applied Sciences, Harvard University, Cambridge, MA, USA. [2]Research Center for Advanced Science and Technology, University of Tokyo, Tokyo, Japan. [3]QuTech, Delft University of Technology, Delft, The Netherlands. [4]Center for Molecular Engineering and Materials Science Division, Argonne National Laboratory, Lemont, IL, USA. [5]Pritzker School of Molecular Engineering, University of Chicago, Chicago, IL, USA. ✉e-mail: kkuruma@g.ecc.u-tokyo.ac.jp; loncar@g.harvard.edu

https://doi.org/10.1038/s41567-024-02697-5

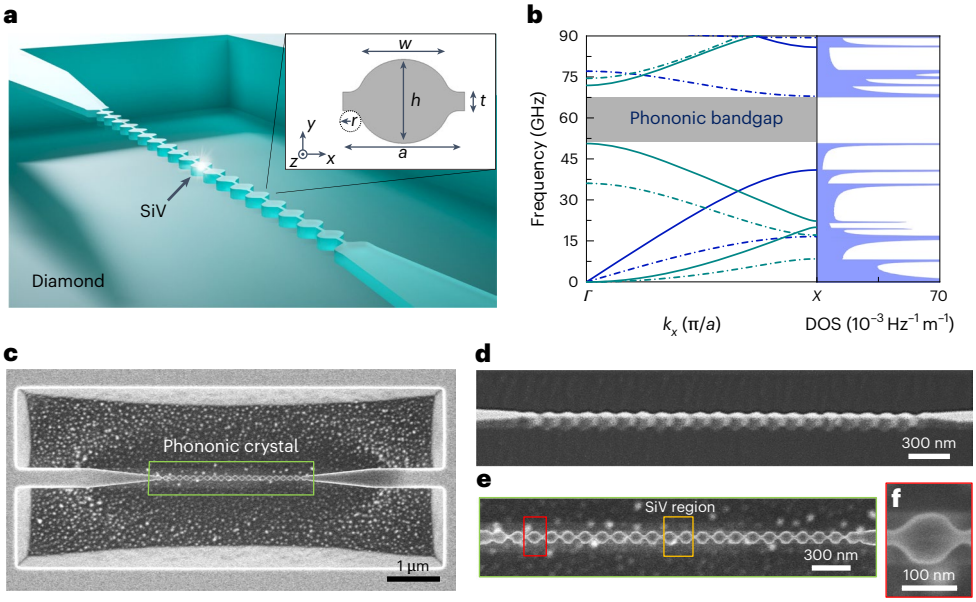

Fig. 1 | PnCs in a single-crystal diamond. a, Illustration of a free-standing PnC supported by tapered wave guides at both ends. Single SiV centres were implanted into PnCs using a deterministic mask implantation technique (Fig. 1e). The inset shows the unit cell of the PnCs, which consists of an elliptical block and two small tethers with a width, *t*. The major and minor axes of the elliptical block and the lattice constant are *w*, *h* and *a*, respectively. The small circle with a radius, *r*, accounts for the rounding of the connection between the block and the tethers due to fabrication imperfection. **b**, Left, simulated phononic band diagram corresponding to the fabricated PnC. The unit cell parameters were obtained by SEM of the fabricated structure (**c**–**f**). The solid (dashed) blue line indicates acoustic modes with even (odd) symmetry along the *y* and *z* axes, whereas the solid (dashed) green line indicates modes with even (odd) symmetry along the *y* axis and odd (even) symmetry along the *z* axis. The grey region indicates a complete phononic bandgap with a centre frequency of 59.1 GHz and width of 17.3 GHz. Right, the corresponding phononic density of states (DOS). **c**–**f**, SEM images showing top (**c**) and tilted (**d**) views of a fabricated suspended PnC consisting of 20 unit cells. An enlarged view of the whole PnC region (**e**) and its unit cell (**f**) are also shown. The fabricated structure has the following parameters, measured using SEM: $w = 96$ nm, $h = 90$ nm, $a = 130$ nm, $t = 22$ nm, $r = 17$ nm and $d = 70$ nm. The SiV-implanted region, indicated by an orange rectangle, overlaps with two blocks and one tether located at the centre of the PnC.

to develop alternative approaches for controlling thermal phonons and their interactions with quantum systems.

Taking inspiration from photonics, an emerging approach relies on engineering the phononic LDOS by fabricating micro/nanostructures. In particular, phononic crystals (PnCs)[18] with periodic modulations of elastic properties have been intensively studied because they can generate phononic bandgaps, a frequency range in which phonons cannot propagate. This is analogous to electronic crystals (semiconductor lattices) that give rise to electronic bandgaps and photonic crystals that support photonic bandgaps for electromagnetic waves[19]. To date, demonstrated PnCs typically operate at relatively low frequencies ($\lesssim$10 GHz) and have mainly been used to realize phononic shields[20] to reduce mechanical losses, as well as in optomechanical cavities[21,22] and wave guides[23,24]. On the other hand, PnCs offer a great opportunity to tailor the interactions between thermal phonons and solid-state quantum systems, such as quantum dots and various colour centres[25], thus improving the system performance by, for example, suppressing decoherence processes induced by high-frequency phonons[11,12,26]. However, tailoring PnCs to specific quantum systems is challenging because it requires pushing the limits of nanofabrication technology while preserving, or ideally improving, the properties of the quantum system. Furthermore, a high degree of control over the frequencies of the targeted phonons is required, which poses additional challenges, particularly when those frequencies are high (50–100 GHz), thereby relying on features in the 10–100 nm range. As a result, previous attempts to control the interaction between bulk/thermal phonons and a quantum system relied on tuning the energy levels of the quantum system[27,28] or lacked the capacity to tailor the LDOS[29,30]. In this study, we demonstrate the engineering of high-frequency phonons and their interactions with single quantum systems using PnCs. We fabricate free-standing diamond PnCs with ~20 nm features, which support a ~20-GHz-wide complete bandgap centred at ~60 GHz, thus reaching previously inaccessible phonon frequencies. We probe the phonon LDOS of our system through changes in the orbital relaxation rates of single negatively charged silicon-vacancy (SiV) colour centres in diamond. SiV centres are known to feature orbital transitions around 50 GHz that are highly sensitive to strain and mechanical vibrations[28,31,32]. We experimentally show that PnCs can suppress the spontaneous emission of phonons from SiV centres, and thus reduce their orbital relaxation rates by more than one order of magnitude compared to SiV centres in bulk. This is analogous to the suppression of spontaneous emission of photons from quantum emitters placed within photonic bandgap structures[33–35]. Furthermore, we show that this large reduction in the relaxation rates using PnCs remains significant up to 20 K, when higher-order phonon processes start to dominate.

Design and fabrication of diamond PnCs

We used free-standing one-dimensional 'block–tether'-type PnCs supported by tapered wave guides, as schematically shown in Fig. 1a. This simple PnC structure is known to support complete bandgaps[36]. The unit cell of the PnCs (inset of Fig. 1a) is composed of an elliptical block and small tethers with thickness $d = 70$ nm and lattice constant $a = 130$ nm. The major (w) and minor (h) axes of the elliptical block are 96 and 90 nm, respectively. To obtain a larger bandgap, we decreased the tether width (t) as much as possible (Supplementary Fig. 3), leading to an increased mass contrast between the elliptical block and the tether. We chose devices with a very small t of ~20 nm for the experiments with SiV centres.

Figure 1b shows the dispersion relation (frequency versus wave vector) for the phonon modes supported by the structure and obtained by simulating the unit cell with its experimentally measured dimensions (Supplementary Information 2) using the finite element

https://doi.org/10.1038/s41567-024-02697-5

method (COMSOL Multiphysics). The band diagram features a large complete phononic bandgap with a width of 17.3 GHz centred at 59.1 GHz. These values are four to ten times greater than those reported previously[20,21,37,38]. Similar to photonic bandgaps, the phononic bandgap results in complete depletion of the phononic LDOS in this frequency range, as shown in the right panel of Fig. 1b. The realization of a wide complete phononic bandgap at high frequencies is important for tailoring the bandgap to quantum systems with high-frequency transitions, such as the SiV centre. Furthermore, the wide bandgap aims to accommodate the inhomogeneous distribution in transition frequencies common in solid-state quantum systems, as well as to mitigate multi-phonon processes over a wide range of high frequencies (discussed later). The robustness of the bandgap against fabrication imperfections is discussed in Supplementary Information 3. The bandgap frequency was chosen to overlap with the orbital ground-state splitting (Δ_{GS}) of a typical low-strain SiV centre (>46 GHz) and thus suppress the spontaneous single-phonon transitions, as detailed in the following section.

The suspended PnCs were fabricated into a single-crystal diamond substrate using top-down reactive ion etching, followed by a quasi-isotropic etching step[39,40] (Methods and Supplementary Information 1). The scanning electron microscopy (SEM) images of the fabricated PnCs are shown in Fig. 1c–f. The PnC structure has a periodicity of ~100 nm and features as small as ~20 nm (Fig. 1f). SiV centres were deterministically incorporated into the centre of the PnC device using a mask implantation technique[41] (Methods). The SiV-implanted area overlaps with the two blocks and one tether located at the centre of the PnC, as illustrated by the orange rectangle in Fig. 1e.

Orbital lifetime measurements for SiV centres

The single SiV centres used to probe the phononic LDOS consist of a silicon atom and two vacancies occupying adjacent lattice sites in the diamond crystal, as schematically shown in Fig. 2a. Figure 2b displays the simplified electronic energy levels of a SiV centre with one of the excited states and two ground states with a splitting of Δ_{GS} (see Supplementary Information 6 for the detailed energy level). This splitting originates from the spin–orbit coupling in the SiV centres, and the typical Δ_{GS} of unstrained SiV centres in bulk is ~50 GHz (ref. 42). The transitions due to single-phonon emission and absorption between the two ground states (green arrows) determine the lifetime of the orbital states ($T_{1,orbit}$), which is the main limitation of the electronic spin coherence time of the SiV centres at around 4 K (refs. 12,43). To measure $T_{1,orbit}$ for our single SiV centres, we performed time-resolved pump–probe measurements at 4.4 K (Methods and Supplementary Fig. 5) with laser pulses resonant with the electronic transition probing the population in state |1> (blue arrow shown in Fig. 2b). Figure 2c shows the pulse sequence in which we sent two successive laser pulses separated by a variable delay τ to perform the initialization and read-out of the orbital state (upper panel). The lower panel shows an example of the measured time-resolved fluorescence for $\tau = 30$ ns: the first laser pulse leads to initialization through optical pumping into state |2>, and the second pulse probes the population into state |1>, recovering via phonon-mediated transitions (green arrows in Fig. 2b). The amount of population recovery was measured from the ratio of the area under the leading edge of the read-out pulse to that of the initialization pulse (blue areas). Figure 2d shows an example of population recovery as a function of τ measured for a single SiV centre in bulk. From the fit of the exponential recovery (Supplementary Information 7), we extracted $T_{1,orbit}$ in bulk to be 34 ± 1 ns, which is comparable to that reported for bulk SiV centres at around 4 K (ref. 42).

SiV orbital degrees of freedom as probes of phononic LDOS

Next, we compared the $T_{1,orbit}$ measured in PnCs to that in bulk as well as suspended diamond nanobeams with the same width and thickness

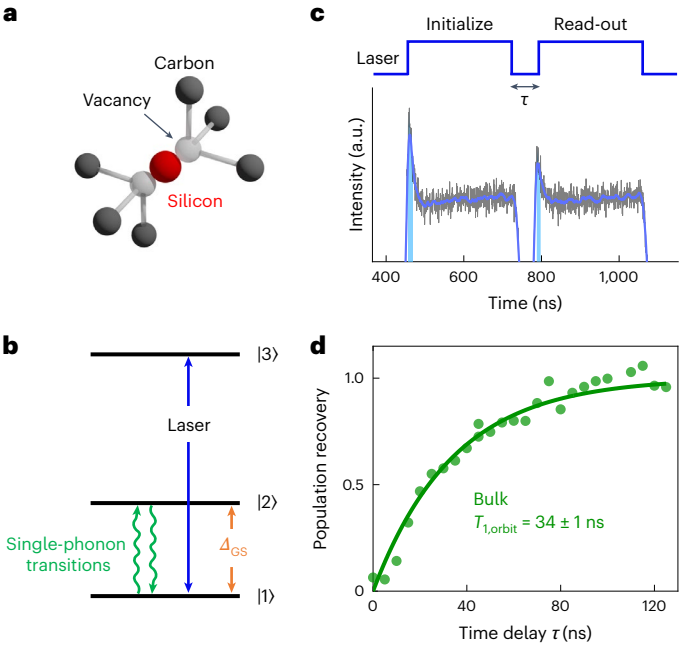

Fig. 2 | Orbital lifetime measurements of single SiV centres. a, Schematic of the atomic structure of the SiV centre in diamond. **b**, Energy level structure of the SiV centre showing frequency splitting between orbital branches in the ground state (Δ_{GS}). The upward and downward spontaneous single-phonon processes between the ground states are indicated by green arrows. The solid blue arrow indicates the laser resonant excitation to one of the energy levels for orbital lifetime measurements. **c**, Pulse sequence for the orbital lifetime measurements, consisting of 300-ns-long initialization and read-out pulses with a time delay (τ) in between (upper panel). An example of a time-trace fluorescence spectrum measured at $\tau = 30$ ns, corresponding to a population recovery of 0.5, for a single SiV centre in bulk (lower panel). The grey and blue lines represent the measured and smoothed data, respectively. A moving-average method was used to reduce noise in the smoothed data. The blue areas indicate a 10-ns-wide integration range used to calculate the ratio between the leading edges and estimate population recovery. The overall steady-state signal was determined by the balance between optical pumping and phonon-induced decay. Note that the fluorescence increase in the steady state was due to power variations across the generated pulse. **d**, Thermalization curve showing the population recovery of state |1> (green dots), calculated as the ratio between the integrated leading edges of the read-out and initialization pulses after subtracting steady-state populations from them (Supplementary Information 7) in the time-trace spectrum as a function of τ, as shown in Fig. 2c. The solid green line is a fitting curve with an exponential function to extract $T_{1,orbit}$ as the 1/e value. The extracted $T_{1,orbit}$ in bulk was 34 ± 1 ns.

as PnCs (Fig. 3a) and fabricated on the same chip. In this experiment, we used low-strain SiV centres with $\Delta_{GS} \approx 60$ GHz, corresponding to our PnC bandgap. Note that we chose such SiV centres after device fabrication and measurements of Δ_{GS} (Supplementary Information 6). Using photoluminescence-based measurements (Methods and Supplementary Information 8), we confirmed that the SiV emission in PnCs was stable enough to perform $T_{1,orbit}$ measurements. Note that the observed optical linewidth was slightly broader than the typical lifetime-limited value[44], but it was still comparable to that of SiVs in nanostructures[45] (Supplementary Information 8). Figure 3b shows the thermalization curves measured for SiV centres with similar Δ_{GS} within the bandgap in PnC (red), nanobeam (blue) and bulk (green). The population recovery observed for SiV in PnC was much slower than that in bulk and nanobeam. The longest $T_{1,orbit}$ among the measured SiV centres within the bandgap is 486 ± 12 ns, which is approximately 18 (15) times longer than the average lifetime for five different SiV centres measured in bulk (nanobeam). This is evidence of significant suppression of the phononic LDOS at ~60 GHz by the bandgap effect. On the

https://doi.org/10.1038/s41567-024-02697-5

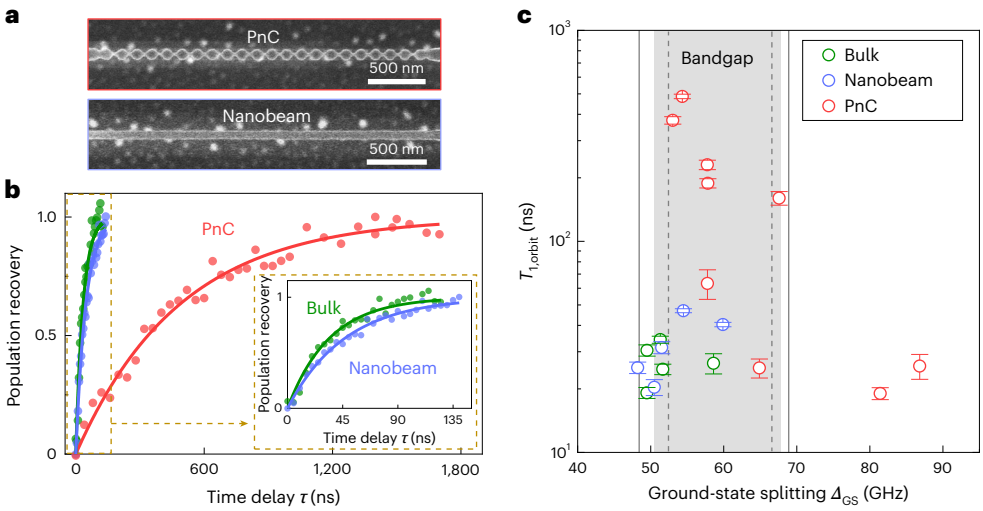

Fig. 3 | Ground-state splitting dependence of SiV orbital lifetimes. **a**, SEM images of a suspended diamond PnC (upper) and a diamond nanobeam (phononic wave guide without PnC) (lower) fabricated on the same chip. **b**, Thermalization curves measured for a single SiV centre in bulk, nanobeam and PnC. The solid lines represent fitting curves based on a single exponential function. The inset shows an enlarged view of the thermalization curves for the bulk and nanobeam. **c**, Measured $T_{1,orbit}$ as a function of Δ_{GS} for SiV centres in different PnC and nanobeam devices with the same device parameters. The data points and error bars represent the fitted $T_{1,orbit}$ and the standard deviation of the fitting, respectively. The grey shaded region corresponds to the calculated phononic bandgap, as shown in Fig. 1e. The grey solid (dashed) lines indicate the uncertainty of the position and size of the bandgap induced by the standard deviation of −3 nm (+3 nm) from the measured tether width t = 22 nm.

other hand, as shown in Fig. 3b, we did not observe a significant change in $T_{1,orbit}$ for the SiV centres in nanobeams relative to bulk despite the modified LDOS induced by their lower dimensionality[30,46] (Supplementary Information 4). This suggests that a complete bandgap is necessary to sufficiently suppress thermal phonons and the resulting phonon-induced relaxation.

We then used SiV centres with different Δ_{GS}, implanted in different devices fabricated using the same geometric parameters, to probe the extent of the phononic bandgap. Figure 3c shows a summary of $T_{1,orbit}$, overlaid with the same calculated phononic bandgap as that shown in Fig. 1b, including the fabrication uncertainty of the PnC parameters (Supplementary Information 3). Overall, the values of $T_{1,orbit}$ for SiV centres with Δ_{GS} within the bandgap tend to be much higher than those in the bulk and nanobeams, further supporting the conclusion that the phonon-induced transitions between ground-state orbitals are largely suppressed by the bandgap effect. The fluctuation of $T_{1,orbit}$ within the bandgap, particularly the lower $T_{1,orbit}$ values, could be due to variations in bandgap size and/or position caused by fabrication imperfection (Supplementary Information 3) or the degradation of the emitters located near the etched sidewalls[30,47]. The finite improvement in $T_{1,orbit}$ is likely due to the contribution of higher-order phonon processes with frequencies outside the phononic bandgap, as discussed next. For further improvement of $T_{1,orbit}$, it might be helpful to use larger complete bandgaps with higher dimensionality, realized in two-dimensional PnCs[20]. To further probe the bandgap, we measured $T_{1,orbit}$ on strained SiV centres with Δ_{GS} outside the bandgap (>70 GHz). As expected, $T_{1,orbit}$ outside the bandgap showed similar values to those measured in the bulk and nanobeams, indicating the realization of a large phononic bandgap of approximately 20 GHz at around 60 GHz.

Temperature-dependent measurements of orbital lifetimes

Finally, we investigated the resilience of phonon suppression to temperature. To this end, we studied the temperature dependence of population recovery by measuring $T_{1,orbit}$ from 4.4 to 20 K. We used the same single SiV centres in the bulk, nanobeam and PnC, as shown in Fig. 3b. Figure 4a shows examples of thermalization curves measured for the SiV centre in the PnC bandgap at six different temperatures. As expected, the population recovery became faster with increasing sample temperature due to the higher thermal population of the residual phononic LDOS. The temperature dependence of the orbital relaxation rates ($\Gamma = 1/T_{1,orbit}$) measured for SiV centres in the bulk, nanobeam and PnC is plotted in Fig. 4b. The Γ measured in bulk tends to increase linearly with temperature because single-phonon processes between the ground-state levels are dominant below 20 K, which is consistent with previously reported observations for bulk SiV centres[12,42]. We also observed a linear temperature dependence of Γ for the SiV centre in a nanobeam while showing a slightly slower speed of increase (0.47 ± 0.02 MHz K^{-1}) compared to bulk (0.68 ± 0.04 MHz K^{-1}). The evolution of Γ for the SiV centre in PnC below 12 K can also be approximated as a linear relationship with temperature, although it shows a much smaller slope of 0.15 ± 0.004 MHz K^{-1}. The difference in the rate of increase in Γ between the PnC and bulk (nanobeam) originated from the differences in the phononic LDOS (Supplementary Fig. 4), indicating that modifying the LDOS is advantageous for suppressing the increase in Γ at elevated temperatures. At temperatures above 12 K, Γ for PnC started to deviate from the single-phonon linear trend, which can be explained by the emergence of two-phonon processes. Among the possible two-phonon processes that can affect solid-state quantum systems, we considered the two-phonon inelastic Raman scattering process[42]. Additional processes, such as elastic Raman scattering, cannot induce an orbital change, whereas an Orbach process would require an additional intermediate state (see the detailed discussion of the model, including the influence of various processes, including a higher-order phonon process, in Supplementary Information 9). Above 12 K, the experimental data can be well fitted by adding a component proportional to T^5 to the fitting curve (red solid curve), as shown in Fig. 4b. This result suggests that the two-phonon inelastic Raman scattering[42] with frequencies outside the bandgap becomes dominant above 12 K, whereas such contributions only become visible above 20 K in bulk[42]. This is due to the large suppression of the single-phonon processes by the PnC bandgap. These results demonstrate the successful suppression of spontaneous single-phonon transitions at high frequencies of around 60 GHz by the PnC bandgap effect. Importantly, the measured $T_{1,orbit}$ for PnC at 20 K was ~30 ns, which is comparable to the average $T_{1,orbit}$ of bulk SiV centres (~27 ns) measured at 4.4 K (dashed grey line

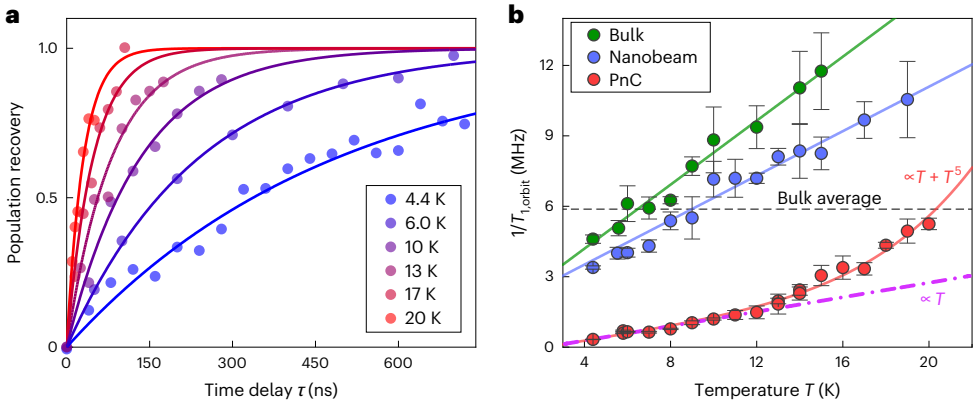

Fig. 4 | Temperature dependence of orbital relaxation rates of single SiV centres. a, Population recovery measured for a single SiV centre in the PnC bandgap at six different temperatures. The solid lines are fitting curves based on a single exponential function to extract the $T_{1,\mathrm{orbit}}$. **b**, Temperature dependence of the measured orbital relaxation rate ($\Gamma = 1/T_{1,\mathrm{orbit}}$) for single SiV centres in bulk (green), nanobeam (blue) and PnC (red). In each case, the SiV centre with the longest $T_{1,\mathrm{orbit}}$ was used for the temperature-dependent measurements. The error bars are standard deviations extracted from a single exponential fitting. The data for the bulk and nanobeam can be fitted with a linear regression of T. For the SiV centre in PnC, the dashed pink line is a linear fit to the experimental data below 12 K. The red solid curve is a fitting with a polynomial function proportional to T and T^5. The dashed grey line indicates the average value for bulk SiV centres measured at 4.4 K.

in Fig. 4b). This indicates that PnCs with a complete bandgap may be useful for increasing the operating temperature of the SiV centres.

Discussion

In summary, we demonstrated phononic LDOS engineering at sub-100 GHz frequencies using diamond PnCs. Our structures, with features down to 20 nm, support a ~20-GHz-wide complete phononic bandgap at ~60 GHz. We used single SiV centres as a phononic probe of the LDOS in the PnCs, as well as in the bulk and nanobeam wave guides used for comparison. As a result of the LDOS control using the bandgap effect, the SiV orbital lifetimes in PnCs are more than one order of magnitude longer than those in bulk and nanobeam wave guides, thereby demonstrating the inhibition of single-phonon processes in the SiV centres. This suppression also allowed us to observe the effects of multi-phonon processes at lower temperatures than in the bulk. These results not only open the possibility of efficiently controlling specific high-frequency phonons of interest for applications in radio-frequency signal processing[48], optomechanics[49], nonlinear phononics[50] and thermoelectrics[51], but also may improve the optical and/or spin properties of solid-state quantum systems at higher temperatures. In the case of the SiV centres, this may lead to improved spin coherence at temperatures higher than millikelvin (see discussion in Supplementary Information 10) because the SiV spin coherence is known to be predominantly limited by phonon-induced orbital relaxation due to strong spin–orbit coupling[27]. Our approach could also be applied to any other solid-state quantum systems that interact with thermal phonons[13,26,52]. We can also expect to realize phononic nanocavities and wave guides based on our PnCs, particularly for enhancing the spontaneous single-phonon emission from quantum emitters, analogous to photonic crystal cavities and wave guides used for enhancing the photon emission of quantum emitters through the Purcell effect[40]. Finally, because our PnC structures are compatible with existing planar photonic and phononic integrated platforms[53], they could be fundamental building blocks for realizing phonon-mediated devices with solid-state quantum emitters and qubits for quantum acoustodynamics[54] and scalable quantum networks[55].

Online content

Any methods, additional references, Nature Portfolio reporting summaries, source data, extended data, supplementary information, acknowledgements, peer review information; details of author contributions and competing interests; and statements of data and code availability are available at https://doi.org/10.1038/s41567-024-02697-5.

References

1. Mirhosseini, M., Sipahigil, A., Kalaee, M. & Painter, O. Superconducting qubit to optical photon transduction. *Nature* **588**, 599–603 (2020).
2. Wollack, E. A. et al. Quantum state preparation and tomography of entangled mechanical resonators. *Nature* **604**, 463–467 (2022).
3. Chu, Y. et al. Quantum acoustics with superconducting qubits. *Science* **358**, 199–202 (2017).
4. Köhler, R. et al. Terahertz semiconductor-heterostructure laser. *Nature* **417**, 156–159 (2002).
5. Scarcelli, G. & Yun, S. H. Confocal Brillouin microscopy for three-dimensional mechanical imaging. *Nat. Photonics* **2**, 39–43 (2008).
6. Lee, G. et al. Piezoelectric energy harvesting using mechanical metamaterials and phononic crystals. *Commun. Phys.* **5**, 94 (2022).
7. Degen, C. L., Reinhard, F. & Cappellaro, P. Quantum sensing. *Rev. Mod. Phys.* **89**, 1–39 (2017).
8. Li, B.-B., Ou, L., Lei, Y. & Liu, Y.-C. Cavity optomechanical sensing. *Nanophotonics* **10**, 2799–2832 (2021).
9. Bienfait, A. et al. Phonon-mediated quantum state transfer and remote qubit entanglement. *Science* **364**, 368–371 (2019).
10. Schuetz, M. J. A. et al. Universal quantum transducers based on surface acoustic waves. *Phys. Rev. X* **5**, 1–30 (2015).
11. Iles-Smith, J., McCutcheon, D. P. S., Nazir, A. & Mørk, J. Phonon scattering inhibits simultaneous near-unity efficiency and indistinguishability in semiconductor single-photon sources. *Nat. Photonics* **11**, 521–526 (2017).
12. Pingault, B. et al. Coherent control of the silicon-vacancy spin in diamond. *Nat. Commun.* **8**, 15579 (2017).
13. Chen, M., Owens, J. C., Putterman, H., Schäfer, M. & Painter, O. Phonon engineering of atomic-scale defects in superconducting quantum circuits. *Sci. Adv.* **10**, 1 (2024).
14. Sukachev, D. D. et al. Silicon-vacancy spin qubit in diamond: a quantum memory exceeding 10 ms with single-shot state readout. *Phys. Rev. Lett.* **119**, 223602 (2017).
15. Noiri, A. et al. Fast universal quantum gate above the fault-tolerance threshold in silicon. *Nature* **601**, 338–342 (2022).

16. Nguyen, C. T. et al. An integrated nanophotonic quantum register based on silicon-vacancy spins in diamond. *Phys. Rev. B* **100**, 165428 (2019).
17. Bradley, C. E. et al. A ten-qubit solid-state spin register with quantum memory up to one minute. *Phys. Rev. X* **9**, 031045 (2019).
18. Kushwaha, M. S., Halevi, P., Dobrzynski, L. & Djafari-Rouhani, B. Acoustic band structure of periodic elastic composites. *Phys. Rev. Lett.* **71**, 2022–2025 (1993).
19. Yablonovitch, E. Inhibited spontaneous emission in solid-state physics and electronics. *Phys. Rev. Lett.* **58**, 2059–2062 (1987).
20. MacCabe, G. S. et al. Nano-acoustic resonator with ultralong phonon lifetime. *Science* **370**, 840–843 (2020).
21. Gomis-Bresco, J. et al. A one-dimensional optomechanical crystal with a complete phononic band gap. *Nat. Commun.* **5**, 1–6 (2014).
22. Ren, H. et al. Two-dimensional optomechanical crystal cavity with high quantum cooperativity. *Nat. Commun.* **11**, 3373 (2020).
23. Fang, K., Matheny, M. H., Luan, X. & Painter, O. Optical transduction and routing of microwave phonons in cavity-optomechanical circuits. *Nat. Photonics* **10**, 489–496 (2016).
24. Zivari, A., Stockill, R., Fiaschi, N. & Gröblacher, S. Non-classical mechanical states guided in a phononic waveguide. *Nat. Phys.* **18**, 789–793 (2022).
25. Aharonovich, I., Englund, D. & Toth, M. Solid-state single-photon emitters. *Nat. Photonics* **10**, 631–641 (2016).
26. Lutz, T. et al. Modification of phonon processes in nanostructured rare-earth-ion-doped crystals. *Phys. Rev. A* **94**, 013801 (2016).
27. Sohn, Y.-I. et al. Controlling the coherence of a diamond spin qubit through its strain environment. *Nat. Commun.* **9**, 2012 (2018).
28. Meesala, S. et al. Strain engineering of the silicon-vacancy center in diamond. *Phys. Rev. B* **97**, 1–14 (2018).
29. Klotz, M. et al. Prolonged orbital relaxation by locally modified phonon density of states for the Si V^- center in nanodiamonds. *Phys. Rev. Lett.* **128**, 153602 (2022).
30. Lutz, T. et al. Effect of the nanopillar diameter on diamond silicon vacancy center spin lifetime. *Opt. Mater. Express* **14**, 226 (2024).
31. Maity, S. et al. Coherent acoustic control of a single silicon vacancy spin in diamond. *Nat. Commun.* **11**, 193 (2020).
32. Maity, S. et al. Mechanical control of a single nuclear spin. *Phys. Rev. X* **12**, 011056 (2022).
33. Ogawa, S., Imada, M., Yoshimoto, S., Okano, M. & Noda, S. Control of light emission by 3D photonic crystals. *Science* **305**, 227–229 (2004).
34. Lodahl, P. et al. Controlling the dynamics of spontaneous emission from quantum dots by photonic crystals. *Nature* **430**, 654–657 (2004).
35. Fujita, M., Takahashi, S., Tanaka, Y., Asano, T. & Noda, S. Simultaneous inhibition and redistribution of spontaneous light emission in photonic crystals. *Science* **308**, 1296–1298 (2005).
36. Safavi-Naeini, A. H. & Painter, O. Design of optomechanical cavities and waveguides on a simultaneous bandgap phononic–photonic crystal slab. *Opt. Express* **18**, 14926 (2010).
37. Graczykowski, B. et al. Phonon dispersion in hypersonic two-dimensional phononic crystal membranes. *Phys. Rev. B* **91**, 075414 (2015).
38. Florez, O. et al. Engineering nanoscale hypersonic phonon transport. *Nat. Nanotechnol.* **17**, 947–951 (2022).
39. Khanaliloo, B., Mitchell, M., Hryciw, A. C. & Barclay, P. E. High-Q/*V* monolithic diamond microdisks fabricated with quasi-isotropic etching. *Nano Lett.* **15**, 5131–5136 (2015).
40. Kuruma, K. et al. Coupling of a single tin-vacancy center to a photonic crystal cavity in diamond. *Appl. Phys. Lett.* **118**, 230601 (2021).
41. Machielse, B. et al. Quantum interference of electromechanically stabilized emitters in nanophotonic devices. *Phys. Rev. X* **9**, 031022 (2019).
42. Jahnke, K. D. et al. Electron–phonon processes of the silicon-vacancy centre in diamond. *New J. Phys.* **17**, 043011 (2015).
43. Rogers, L. J. et al. All-optical initialization, readout and coherent preparation of single silicon-vacancy spins in diamond. *Phys. Rev. Lett.* **113**, 263602 (2014).
44. Rogers, L. J. et al. Multiple intrinsically identical single-photon emitters in the solid state. *Nat. Commun.* **5**, 4739 (2014).
45. Evans, R. E., Sipahigil, A., Sukachev, D. D., Zibrov, A. S. & Lukin, M. D. Narrow-linewidth homogeneous optical emitters in diamond nanostructures via silicon ion implantation. *Phys. Rev. Appl.* **5**, 044010 (2016).
46. Nishiguchi, N., Ando, Y. & Wybourne, M. N. Acoustic phonon modes of free-standing rectangular wires. *Superlattices Microstruct.* **22**, 213–216 (1997).
47. Liu, J. et al. Single self-assembled InAs/GaAs quantum dots in photonic nanostructures: the role of nanofabrication. *Phys. Rev. Appl.* **9**, 064019 (2018).
48. Shin, H. et al. Control of coherent information via on-chip photonic–phononic emitter–receivers. *Nat. Commun.* **6**, 6427 (2015).
49. Aspelmeyer, M., Kippenberg, T. J. & Marquardt, F. Cavity optomechanics. *Rev. Mod. Phys.* **86**, 1391–1452 (2014).
50. Burgwal, R. & Verhagen, E. Enhanced nonlinear optomechanics in a coupled-mode photonic crystal device. *Nat. Commun.* **14**, 1526 (2023).
51. Nomura, M. et al. Review of thermal transport in phononic crystals. *Mater. Today Phys.* **22**, 100613 (2022).
52. Hanson, R. & Awschalom, D. D. Coherent manipulation of single spins in semiconductors. *Nature* **453**, 1043–1049 (2008).
53. Xu, X.-B., Wang, W.-T., Sun, L.-Y. & Zou, C.-L. Hybrid superconducting photonic–phononic chip for quantum information processing. *Chip* **1**, 100016 (2022).
54. Bolgar, A. N. et al. A phononic crystal coupled to a transmission line via an artificial atom. *Commun. Phys.* **3**, 207 (2020).
55. Lemonde, M.-A. et al. Phonon networks with silicon-vacancy centers in diamond waveguides. *Phys. Rev. Lett.* **120**, 213603 (2018).

Methods

Device fabrication

We used a high-purity (nitrogen concentration less than 5 ppb) electronic-grade single-crystal diamond (Element Six Corporation) that was etched using argon/chlorine followed by oxygen plasma to remove the surface-damaged layer caused by diamond polishing. The diamond was then cleaned using a 1:1:1 boiling triacid mixture of perchloric, nitric and sulfuric acids. We used a mask implantation technique to precisely implant the SiV centres in the desired implantation spots using polymethyl methacrylate resist masks. We created a rectangular aperture (~225 × 300 nm) in polymethyl methacrylate, which defines the implantation spot; silicon ions were implanted only in this area. As a result of the annealing (see below) and PnC fabrication process (Supplementary Information 1), SiV centres can only be found in two blocks and one tether at the centre of the PnCs (within the orange rectangle in Fig. 1e). It is unclear whether the SiV centres are located in the block or tether due to the uncertainty of ion implantation. Details of the mask fabrication can be found in our previous work[41]. After forming the implantation mask on the diamond, silicon ions (Si^+) were implanted with an energy of 50 keV. The resulting mean ion range was ~35 nm from the surface with a straggling of 8 nm, as simulated by the software package Stopping and Range of Ions in Matter. We chose a relatively low ion implantation dose (5×10^{11} ions per cm^2) to obtain approximately zero to one SiV centre per PnC device. The SiV centres were then generated by a high-temperature (1,100 °C) high-vacuum annealing procedure followed by the same boiling triacid cleaning, as described previously. The PnCs were patterned into the bulk diamond containing SiV centres by electron beam lithography and dry etching. The typical alignment accuracy between the SiV implantation spot and the PnCs is on the order of tens of nanometres, which is mainly determined by our electron beam lithography based on alignment makers. To realize free-standing PnCs, we used a quasi-isotropic etching technique to undercut the PhC slab. Details of the fabrication steps can be found in Supplementary Information 1. We fabricated 64 PnC devices with the same parameters, 16 of which had a single SiV. Finally, we used nine PnC devices for orbital lifetime measurements.

Photoluminescence measurements

The diamond sample was mounted on a closed-cycle liquid helium cryostat (attoDRY800) and cooled to 4.4 K. A continuous-wave (CW) 520-nm laser diode (Thorlabs LP520-SF15) was used to pump the sample off-resonantly. The zero-phonon-line (ZPL) emission from single SiV centres in the sample was collected using an objective lens (0.9 numerical aperture × 100) and sent to a spectrometer equipped with a Si charge-coupled device camera to spectrally resolve the ZPLs. For photoluminescence excitation measurements, we used a tunable CW Ti:sapphire laser (M Squared SolsTiS) for resonant excitation of the SiV ZPLs. The photoluminescence excitation emission was collected from the phonon sideband above 750 nm and sent to an avalanche photodiode (Excelitas) to measure the photon counts. The frequency of the tunable laser was stabilized by continuous feedback using a wave-meter (HighFinesse WS7). The CW 520-nm laser was periodically pulsed by a digital delay generator (SRS DG645) to repump the SiV centres into a negatively charged state. A schematic of the optical measurement setup can be found in Supplementary Information 5.

Orbital lifetime measurements

We implemented a two-pulse sequence to measure the orbital lifetime by pulsing our tunable CW Ti:sapphire laser with an acousto-optic modulator (AA Opto-Electronic). The acousto-optic modulator was driven using an arbitrary waveform generator (Tektronix AWG70001A) through a radio frequency switch (Mini-Circuits ZASWA2-50DR-FA+) with a voltage-controlled oscillator (Mini-Circuits ZX95-209-S+). The laser frequency was stabilized using continuous feedback from a wave-meter (HighFinesse WS7). A pulsed 520-nm laser was also used to keep the negatively charged state of the SiV centres. A time-correlated single-photon counting system (PicoHarp 300) with a superconducting nanowire single-photon detector or avalanche photodiode was used to detect the photon counts from the phonon-sideband emission of the SiV centres. For temperature-dependent measurements, the sample temperature was tuned using a local heater attached to the sample holder and stabilized by continuous feedback with a proportional–integral–differential controller.

Data availability

All other data relevant to this study are available from the corresponding authors upon reasonable request. Source data are provided with this paper.

Code availability

The code used for this study is available from the corresponding authors upon reasonable request.

Acknowledgements

We thank S. Iwamoto for technical support, and R. Anufriev and R. Yanagisawa for their helpful discussions. This study was supported by ONR (grant no. N00014-20-1-2425), ARO MURI (grant no. W911NF1810432), NSF STC (grant no. DMR-1231319) and NSF ERC (grant no. EEC-1941583). K.K. acknowledges the financial support from the JSPS Overseas Research Fellowships (project no. 202160592). B.P. acknowledges support through a Marie Skłodowska-Curie fellowship from the European Union's Horizon 2020 research and innovation programme under grant agreement no. 840968 (COHESiV) and support from the US Department of Energy, Office of Basic Energy Sciences, Materials Science and Engineering Division. C.C. acknowledges support from the A*STAR National Science Scholarship. This study was conducted in part at the Center for Nanoscale Systems, Harvard University.

Author contributions

M.L. conceived the project. K.K. and C.C. performed the numerical simulations with the help of M.H. K.K. designed the device. B.P. prepared the diamond sample. K.K. fabricated the device with the help of C.C. and W.D. K.K., B.P., M.H., G.D.J. and C.J.X. carried out the measurements with the help of D.R.A., C.J.X., M.Y. and N.S. K.K. analysed the data. K.K. and B.P. wrote the paper, with contributions from all authors. M.L. supervised the project.

Competing interests

The authors declare no competing interests.

Additional information

Supplementary information The online version contains supplementary material available at https://doi.org/10.1038/s41567-024-02697-5.

Correspondence and requests for materials should be addressed to Kazuhiro Kuruma or Marko Lončar.